Supersonic reaction front propagation initiated by a hot spot in *n*-heptane/air mixture with multistage ignition

Peng Dai, Zheng Chen*

SKLTCS, Department of Mechanics and Engineering Science, College of Engineering, Peking University, Beijing 100871, China

ARTICLE INFO

ABSTRACT

For large hydrocarbon fuels such as *n*-heptane, multistage ignition occurs at low initial temperature. Therefore, multiple pressure pulses produced by multistage ignition and complicated reaction–pressure wave interactions are expected to happen during autoignition and reaction front propagation initiated by a hot spot. In this study, 1D simulations are conducted for *n*-heptane/air mixture with three ignition stages respectively caused by low-, intermediate- and high-temperature chemistries. Multiple pressure waves, shock waves, and detonation waves are identified and they are found to be generated by heat release from different ignition stages and reaction–pressure wave interactions. The thermal states of flow particles at different initial locations are tracked and analyzed; and the mechanism for the development of multiple shock waves and detonation waves is discussed. With the change of temperature gradient inside the hot spot or the hot spot size, such interactions can be strengthened or weakened and thereby the mode of supersonic reaction front propagation changes. Furthermore, both planar and spherical configurations are considered and the curvature effects are examined. It is found that in spherical configuration, the pressure wave caused by intermediate-temperature ignition is not strong enough to induce a second detonation wave as that in planar configuration.

© 2015 The Combustion Institute. Published by Elsevier Inc. All rights reserved.

1. Introduction

High compression ratio helps to improve thermal efficiency in spark ignition engines (SIEs) [1]. However, the tendency of knock increases greatly with compression ratio and currently knock is a severe constraint for downsizing SIEs with turbocharging [1–4]. Therefore, engine knock has received great attention recently [5–7]. It is generally accepted that knock in SIEs is caused by end-gas autoignition [1] and that the coupling between chemical reaction and pressure wave plays an important role in knock formation [5,8–10]. As mentioned by Wang et al. [10], "*knocking is still at an early stage of understanding*". Therefore, in order to understand knock mechanism, studies on various autoignition modes and reaction–pressure wave interaction are still needed.

Zel'dovich et al. [11,12] first analyzed different autoignition modes caused by non-uniform reactivity (i.e., a spatial distribution of ignition delay time). They found that detonation can develop at certain reactivity gradient. In the following decades, many studies were conducted to verify and to extend this theory using simplified one- or two-step kinetic models [13–17] or detailed reaction models [18–24]. More recenctly, Im et al. [54] have proposed a regime diagram for au-

toignition of homogeneous reactant mixtures with turbulent velocity and temperature fluctuations; and Grogan et al. [55] have developed an ignition regime diagram considering the competition between turbulent, chemical, and heat transfer effects in rapid compression machines. In these studies, the hot spot model with linear temperature distribution was popularly used and detonation was indeed observed at certain temperature gradient. However, only simplified chemistry models (one- or two-step chemistry) or simple fuels (such as H_2, CO and CH_4) were considered. Therefore, the chemistry considered in previous studies is greatly different from that of large hydrocarbon fuels used in SIEs, for which low-temperature chemistry and negative-temperature coefficient (NTC) phenomenon are involved.

In the literature, only a few studies considered autoignition and combustion modes of large hydrocarbon fuels with low-temperature chemistry. For examples, Ju et al. [25] investigated the ignition and flame propagation modes in *n*-heptane/air mixture and identified different combustion regimes caused by low- and high-temperature chemistries; Martz et al. [26] studied the combustion regime of a reacting front propagating into an auto-igniting *iso*-octane mixture; Sun et al. [27] found that low temperature ignition can cause strong pressure wave and flame oscillation in concentration-stratified *n*-heptane/air mixtures; and Im and coworkers [28–33] systematically examined the effects of turbulence and temperature inhomogeneity on autoignition processes of different fuels with/without low temperature chemistry. However, in all aforementioned studies, shock wave

and detonation caused by reaction–pressure wave interaction were not observed. Only in our recent work [24], different supersonic autoignition modes including shock wave and detonation were identified for *n*-heptane/air mixture within the NTC regime. However, in [24] we did not focus on multistage ignition or its influence on modes of supersonic reaction front propagation for *n*-heptane/air at low initial temperature.

For large hydrocarbon fuels such as *n*-heptane, multistage ignition occurs at low initial temperature. Heat release during different ignition stages might produce different pressure pulses. Therefore, complicated reaction–pressure wave interactions are expected to happen. This was not investigated before and will be focused on in the present work. Although planar and spherical configurations were considered in previous studies, the geometry/curvature effects on supersonic reaction front propagation are still not well understood and will be examined here.

Therefore, based on above discussion, the objectives of the present study are two-fold. First, we investigate the supersonic reaction front propagation initiated by a hot spot in *n*-heptane/air mixture with multistage ignition. Pressure waves generated by different ignition stages are identified and their influence on modes of supersonic autoignition front propagation is examined. Second, we study the difference between ignition behaviors in planar and spherical configurations. The curvature effects in spherical configuration which weaken pressure waves and detonation waves are assessed.

It should be emphasized that the present work is different from [25] in three aspects: (1) in [25] a hot kernel of 1400 K was used to mimic spark assisted compression ignition while here a hot spot with linear temperature gradient is used to initialize the reaction front propagation; (2) as a result, supersonic reaction front was not observed in [25] while it is observed here; and (3) multiple pressure/shock/detonation waves generated by heat release from different ignition stages are identified and analyzed here through tracking the thermal states of flow particles at different initial locations while this was not found/conducted in [25].

The paper is organized as follows: in Section 2, the numerical model and methodologies are presented; then in Section 3, three ignition stages of *n*-heptane/air mixture at low initial temperature are identified and the critical temperature gradient is discussed; the interaction among different ignition stages and pressure waves as well as the geometry/curvature effects are investigated in Section 4; and finally, the conclusions are summarized in Section 5.

2. Numerical model and methodologies

2.1. Numerical model

In order to investigate the supersonic reaction front propagation and the interaction among different ignition stages and pressure waves, we simulate the transient autoignition process initiated by a hot spot for *n*-heptane/air mixture in a 1D closed chamber.

The transient autoignition process is simulated using the in-house code A-SURF [24,34,35]. A-SURF solves the conservation equations (including the unsteady Navier–Stokes equations as well as the energy and species conservation equations) for 1D, adiabatic, multicomponent, reactive flow in a planar or spherical coordinate:

$$\frac{\partial U}{\partial t} + \frac{\partial F(U)}{\partial x} + N\frac{G(U)}{x} = F_v(U) + S_R \tag{1}$$

where N is the geometry factor ($N = 0$ and 2 for planar and spherical coordinates, respectively); and t and x are respectively the temporal and spatial coordinates (x should be replaced by r for spherical configuration). In Eq. (1), the vectors U, $F(U)$, $G(U)$, $F_v(U)$, and S_R are

defined as:

$$U = \begin{pmatrix} \rho Y_1 \\ \rho Y_2 \\ \vdots \\ \rho Y_n \\ \rho u \\ E \end{pmatrix}, \quad F(U) = \begin{pmatrix} \rho u Y_1 \\ \rho u Y_2 \\ \vdots \\ \rho u Y_n \\ \rho u^2 + P \\ (E+P)u \end{pmatrix}, \quad G(U) = \begin{pmatrix} \rho u Y_1 \\ \rho u Y_2 \\ \vdots \\ \rho u Y_n \\ \rho u^2 \\ (E+P)u \end{pmatrix}$$

$$F_v(U) = \begin{pmatrix} -x^{-N}(x^N \rho Y_1 V'_1)_x \\ -x^{-N}(x^N \rho Y_2 V'_2)_x \\ \vdots \\ -x^{-N}(x^N \rho Y_n V'_n)_x \\ x^{-N}(x^N \tau_1)_x - N\tau_2/x \\ x^{-N}q_x + \Phi \end{pmatrix}, \quad S_R = \begin{pmatrix} \omega_1 \\ \omega_2 \\ \vdots \\ \omega_n \\ 0 \\ 0 \end{pmatrix} \tag{2}$$

In Eq. (2), ρ is the density, Y_k the mass fraction of species k, u the flow velocity, and E the total energy per unit mass. The subscript x in $F_v(U)$ stands for the partial derivative with respect to x. Instead of solving the continuity equation, the species conservation equations for all n species are solved in A-SURF. The continuity equation is recovered from the summation of all species conservation equations.

In the species conservation equations, ω_k and V'_k are the production rate and diffusion velocity of species k, respectively. The production rate ω_k is specified via collection of elementary reactions

$$\omega_k = M_k \sum_{j=1}^{n_r} \left\{ (v''_{k,j} - v'_{k,j}) \left[K_{f,j} \prod_{k=1}^{n} \left(\frac{\rho Y_k}{M_k} \right)^{v'_{k,j}} \right. \right.$$

$$\left. \left. - K_{b,j} \prod_{k=1}^{n} \left(\frac{\rho Y_k}{M_k} \right)^{v''_{k,j}} \right] \right\} \tag{3}$$

where M_k is the molecular weight of species k; n_r is the total number of elementary reactions; $v'_{k,j}$ and $v''_{k,j}$ are the molar stoichiometric coefficients of species k in reaction j; and $K_{f,j}$ and $K_{b,j}$ are the forward and reverse reaction rate of reaction j. The forward reaction rate for each elementary reaction is usually modeled using the empirical Arrhenius law

$$K_{f,j} = A_{f,j} T^{\beta_j} \exp\left(-\frac{E_j}{RT} \right) \tag{4}$$

where $A_{f,j}$ is the pre-exponential constant, β_j the temperature exponent, and E_j the activation energy. The reverse reaction rate can be obtained from chemical equilibrium constant and the forward reaction rate. These parameters ($A_{f,j}$, β_j, E_j) are given in the chemical mechanism and the reaction rates are calculated using the CHEMKIN package [36].

In simulation we use the skeletal mechanism for *n*-heptane oxidation [37]. It consists of 44 species and 112 elementary reactions. This mechanism has been demonstrated to be able to accurately predict ignition (including the NTC regime) and flame propagation in *n*-heptane/air mixtures at a broad range of temperature and pressure [37].

The diffusion velocity of species k is composed of three parts:

$$V'_k = V'_{k,Y} + V'_{k,T} + V'_{k,C} \tag{5}$$

$V'_{k,Y}$ is the ordinary diffusion velocity given by the mixture-averaged formula [38]:

$$Y_k V'_{k,Y} = -D_{km} \frac{1}{\bar{M}} \frac{\partial (Y_k \bar{M})}{\partial x} \tag{6}$$

where D_{km} is the mixture-averaged diffusion coefficient of species k and $\bar{M}$ is the mean molecular weight of the mixture.

$V'_{k,T}$ is the thermal diffusion velocity, which is included only for low molecular weight species (hydrogen atom and hydrogen molecule):

$$Y_k V'_{k,T} = -D_{km}\Theta_k \frac{M_k}{\bar{M}T}\frac{\partial T}{\partial x} \tag{7}$$

where Θ_k is the thermal diffusion ratio of species k.

The correction velocity $V'_{k,C}$ is included to ensure the compatibility of species and mass conservation equations [38]. It is determined by the requirement of

$$\sum_{k=1}^{n}(Y_k V'_k) = 0 \tag{8}$$

In the momentum equation, P is the pressure and the viscous stresses, τ_1 and τ_2, are

$$\tau_1 = 2\mu\frac{\partial u}{\partial x} - \frac{2}{3}\mu\frac{1}{x^N}\frac{\partial(x^N u)}{\partial x}, \quad \tau_2 = 2\mu\frac{u}{x} - \frac{2}{3}\mu\frac{1}{x^N}\frac{\partial(x^N u)}{\partial x} \tag{9}$$

where μ is the dynamic viscosity of the mixture.

In the energy conservation equation, the total energy, E, is defined through

$$E = -P + \rho u^2/2 + \rho h, \quad h = \sum_{k=1}^{n}(Y_k h_k), \quad h_k = h_{k,0} + \int_{T_0}^{T} C_{P,k}(T)dT \tag{10}$$

where T is the temperature, h_k the enthalpy of species k, $h_{k,0}$ the species enthalpy of formation at the reference temperature T_0, and $C_{P,k}$ the specific heat of species k at constant pressure. The heat flux is

$$q = x^N\left[\lambda\frac{\partial T}{\partial x} - \rho\sum_{k=1}^{n}(h_k Y_k V'_k)\right] \tag{11}$$

where λ is the thermal conductivity of the mixture. In the energy equation, the viscous dissipation rate is

$$\Phi = \mu\left\{2\left(\frac{\partial u}{\partial x}\right)^2 + 2N\left(\frac{u}{x}\right)^2 - \frac{2}{3}\left[\frac{1}{x^N}\frac{\partial(x^N u)}{\partial x}\right]^2\right\}$$
$$+ u\left[\frac{1}{x^N}\frac{\partial(x^N\tau_1)}{\partial x} - N\frac{\tau_2}{x}\right] \tag{12}$$

The pressure can be obtained from the density, temperature and mean molecular weight using the equation of state for an ideal gas

$$P = \frac{\rho RT}{\bar{M}} \tag{13}$$

where $R = 8.314$ J/(mol K) is the universal gas constant.

The thermodynamic and transport properties in Eqs. (6)–(13) are evaluated using the CHEMKIN and TRANSPORT packages [36,38] interfaced with A-SURF. It is noted that the present model is simplified by not including the effects of multicomponent diffusion and bulk viscosity.

In the model we consider transient autoignition initiated by a hot spot in a 1D closed chamber. The model is shown schematically in Fig. 1. The hot spot located near the left boundary is modelled by a linear temperature distribution with negative gradient. The initial temperature distribution is:

$$T_0(x) = T(t=0,x) = \begin{cases} T_m + \left(x - \frac{x_s}{2}\right)\frac{dT_0}{dx} & \text{for } 0 \leq x \leq x_s \\ T_m + \frac{x_s}{2}\frac{dT_0}{dx} & \text{for } x \geq x_s \end{cases} \tag{14}$$

where x_s is the hot spot size, T_m is the initial local temperature at $x = 0.5x_s$, and dT_0/dx is the negative temperature gradient inside the hot spot (dT_0/dx is a constant to be specified). Stoichiometric
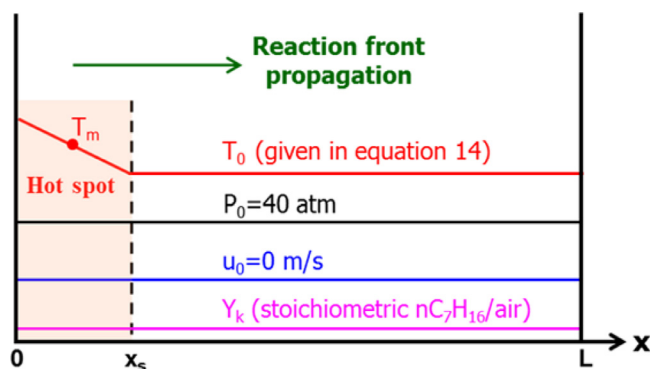

Fig. 1. Schematic of reaction front propagation in a 1D closed chamber with the length of L. The initial conditions are also shown. For the spherical configuration, x should be replaced by r.

n-heptane/air mixture at the initial pressure of $P_0 = 40$ atm is considered. The mixture is static at the beginning (i.e., $u_0 = 0$ m/s). We consider the transient autoignition process occurring in a 1D closed chamber which has the length of $L = 10$ cm. Adiabatic, nonpenetrative, reflective boundary conditions are adopted for both boundaries at $x = 0$ and $x = L$:

$$u = 0, \quad \frac{\partial T}{\partial x} = \frac{\partial Y_k}{\partial x} = \frac{\partial P}{\partial x} = 0 \tag{15}$$

It is noted that in this study the spatial coordinates for both planar and spherical configurations are denoted by the same symbol x. Therefore, x should be replaced by r in spherical configuration.

2.2. Numerical methods

The finite volume method is used to discretize the governing Eq. (1). The second-order accurate, Strang splitting fractional-step procedure [39] is utilized to separate the time evolution of the stiff reaction term S_R from that of the convection and diffusion terms. In the first fractional step, the non-reactive flow is solved:

$$\left.\begin{array}{l} \text{PDE}: \dfrac{\partial U}{\partial t} + \dfrac{\partial F(U)}{\partial x} + N\dfrac{G(U)}{x} = F_v(U) \\ \text{IC}: U(x,t^n) = U^n \end{array}\right\} \Rightarrow \bar{U}^{n+1} \tag{16}$$

The chemistry is solved in the second fractional step for a homogeneous system at each grid

$$\left.\begin{array}{l} \text{ODE}: \dfrac{dU}{dt} = S_R(U) \\ \text{IC}: \bar{U}^{n+1} \end{array}\right\} \Rightarrow U^{n+1} \tag{17}$$

The two steps given by Eqs. (14) and (15) are denoted by operator $C^{(t)}$ and operator $S^{(t)}$, respectively. Based on the above splitting, the solution can be evolved from its initial value U^n at time t^n, by one time step of size Δt, to a value U^{n+1} at time $t^{n+1} = t^n + \Delta t$,

$$U^{n+1} = S^{\Delta t/2}C^{\Delta t}S^{\Delta t/2}(U^n) \tag{18}$$

For the C operator, the Runge–Kutta, MUSCL-Hancock, and central difference schemes, all of second-order accuracy, are employed for the calculation of temporal integration, convective flux, and diffusive flux, respectively. In the S operator, the chemistry is solved in the second fractional step using the VODE solver [40]. The complicated chemistry can be efficiently handled in A-SURF using the algorithms developed by Gou et al. [41,42].

A multi-level, dynamically adaptive mesh refinement algorithm is used in A-SURF to ensure adequate numerical resolution of the reaction zone, pressure wave, shock wave, and detonation wave [24,34,35]. The reaction zone, pressure wave, shock wave, and detonation wave are always covered by the finest mesh with the width
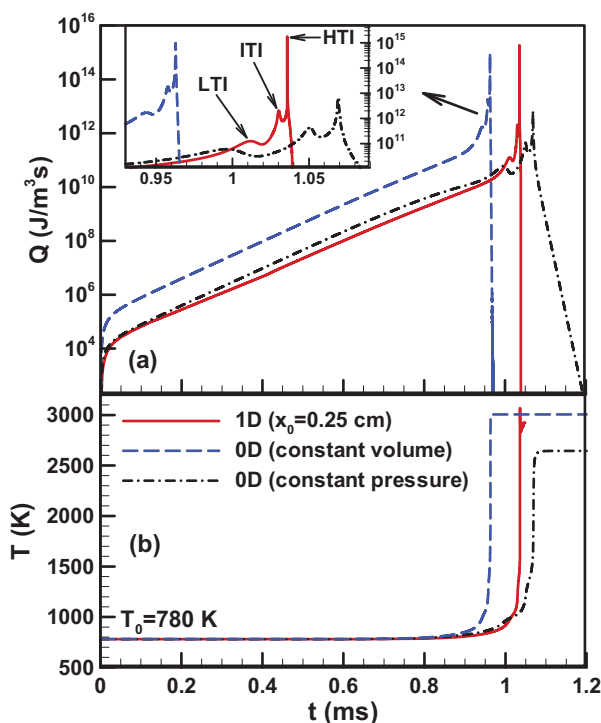
Fig. 2. Temporal evolution of (a) heat release rate and (b) temperature during 0D homogeneous ignition processes for stoichiometric nC_7H_{16}/air mixture at $T_0 = 780$ K and $P_0 = 40$ atm. The results at the midpoint of a hot spot in 1D planar configuration ($\xi = 4$, $x_s = 0.5$ cm, $T_m = 780$ K, $P_0 = 40$ atm) are also shown for comparison. The inset indicates that there are three ignition stages: low-temperature ignition (LTI), intermediate-temperature ignition (ITI), and high-temperature ignition (HTI).

of 2 μm. Explicit method is used for temporal integration and the time step is 4×10^{-10} s. A-SURF has been successfully used in previous studies on ignition and flame propagation (e.g., [43–48]); and it has been demonstrated that A-SURF can capture the propagation of flame, shock wave and detonation wave (see the supplementary documents of Refs. [24,34]).

3. Zero dimensional homogenous ignition

3.1. Multi-stage homogeneous ignition

For large hydrocarbon fuels, ignition is usually dominated by different chemical paths at different temperature ranges; thereby multiple ignition stages may appear [49–51]. Figure 2 shows the temporal evolution of heat release rate and temperature during 0D homogeneous ignition processes at constant-volume and constant-pressure conditions. The results for the ignition process at the midpoint inside a hot spot in 1D planar configuration are also shown for comparison. The initial pressure and temperature of these three cases are the same: $P_0 = 40$ atm and $T_0 = 780$ K which is below the NTC regime (see Fig. 3). The inset of Fig. 2 shows three ignition stages as indicated by three local peaks of heat release rate. Similar three-stage ignition process was also observed for DME/air mixture [51]. These three ignition stages are respectively dominated by low-, intermediate- and high-temperature chemistries [50,51]. Therefore, they are referred to as the low-temperature ignition (LTI), intermediate-temperature ignition (ITI), and high-temperature ignition (HTI), respectively.

Moreover, Fig. 2 shows that the non-homogeneous ignition process at the midpoint of the hot spot stays between the 0D homogeneous ignition processes at constant-volume and constant-pressure. This is because the pressure pulse induced by local heat release propagates outwardly at sound speed, which makes the non-homogeneous ignition process behave between isochoric and
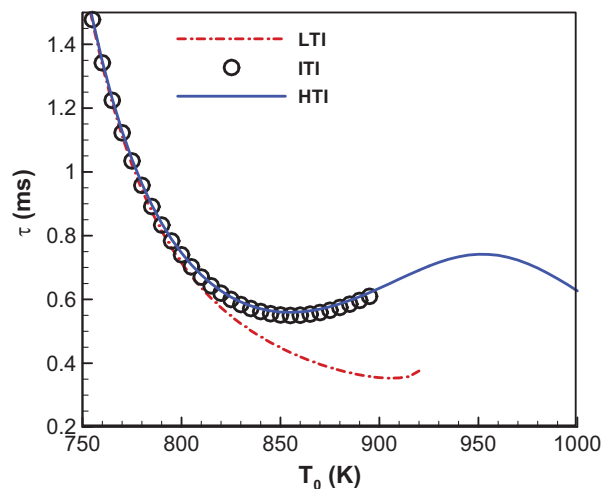
Fig. 3. Change of constant-volume homogeneous ignition delay time with the initial temperature for stoichiometric nC_7H_{16}/air mixture at $P_0 = 40$ atm. The results for three ignition stages, LTI, ITI, and HTI, are plotted.

isobaric homogeneous ignition processes. Similar phenomenon was observed in the simulation conducted by Kurtz and Regele [17].

We define the ignition delay times for these three ignition stages, LTI, ITI and HTI, based on the local maximum heat release rate. The homogeneous ignition delay times are plotted in Fig. 3. The ignition delay time of LTI is shown to be non-monotonic and there exists a minimum value around 900 K. This non-monotonic trend was explained by Zhao and Law [52]. (It is noted that in [52] 0D homogeneous ignition and 1D counterflow non-premixed ignition were studied and the focus was on the first-stage ignition delay. Therefore, the work in [52] is different from present study which investigates multiple shock and detonation waves generated by heat release from different ignition stages and their interactions with pressure waves.) Moreover, Fig. 3 shows that the ignition delay times of LTI, ITI and HTI are very close when $T_0 \leq 820$ K, and that the difference between the ignition delay times of LTI and ITI becomes apparent only when the initial temperature is above 820 K. Since the global ignition delay time for the entire ignition process is equal to the ignition delay time of HTI (i.e., $\tau = \tau_{HTI}$), Fig. 3 indicates that the NTC regime for stoichiometric nC_7H_{16}/air mixture at $P_0 = 40$ atm is $850 \leq T_0 \leq 955$ K.

3.2. Critical temperature gradient

The spatial temperature non-uniformity in the hot spot causes a distribution of local ignition delay time, which leads to sequential autoignition events [12,20]. Therefore, the linear temperature distribution in the hot spot, as shown in Fig. 1, can generate an autoignition wave (or reaction front). Its propagation speed, u_a, is inversely proportional to the gradient of the ignition delay time [12,20]:

$$u_a = \left(\frac{d\tau}{dx} \right)^{-1} = \left(\frac{d\tau}{dT_0} \cdot \frac{dT_0}{dx} \right)^{-1} \tag{19}$$

According to Zel'dovich [12], when the autoignition front propagates at the sound speed, a, it can be coupled with the pressure wave generated by local heat release and the mutual reinforcement between them may lead to detonation development. The temperature gradient at which $u_a = a$ is defined as the critical temperature gradient [20]. According to Eq. (19) and the requirement of $u_a = a$, the critical temperature gradient is [20]:

$$\left(\frac{dT_0}{dx} \right)_c = \left(a \frac{d\tau}{dT_0} \right)^{-1} \tag{20}$$
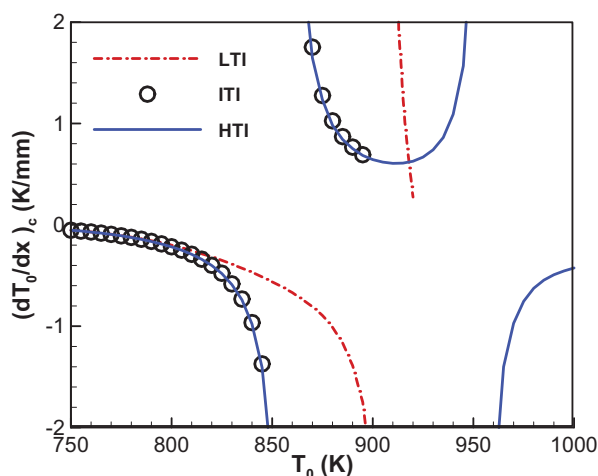
Fig. 4. Change of critical temperature gradient with the initial temperature for stoichiometric nC_7H_{16}/air mixture at $P_0 = 40$ atm. The results for three ignition stages, LTI, ITI, and HTI, are plotted.

Figure 4 plots the critical temperature gradient for all three ignition stages. It is observed that the critical temperature gradient for LTI is different from those for ITI and HTI when $T_0 > 820$ K. However, the critical temperature gradients for different ignition stages are shown to be close to each other when the initial temperature is below 820 K. This indicates that at some proper temperature gradient (not necessarily to be the critical temperature gradient itself, as explained in [20]), all three ignition stages may couple with the corresponding pressure waves and thus lead to strong chemical–acoustic interactions.

4. One dimensional ignition from a hot spot

In NTC regime with $850 \leq T_0 \leq 955$ K, the critical temperature gradient is positive (see Fig. 4) and thereby reaction front propagation can be induced only by a cool spot. This was investigated in our previous study [24]. Here we focus on supersonic reaction front propagation initiated by a hot spot with the initial temperature around 780 K, which is below the NTC regime. Unless otherwise specified, hot spots with $T_m = 780$ K and $x_s = 0.5$ cm in both 1D planar and spherical configurations are considered.

The non-dimensional temperature gradient of the hot spot is introduced as [20]:

$$\xi = \frac{dT_0}{dx} \bigg/ \left(\frac{dT_0}{dx}\right)_c \tag{21}$$

where the critical temperature gradient, $(dT_0/dx)_c = -0.12$ K/mm, is evaluated at $T_m = 780$ K (at which the critical temperature gradients for LTI, ITI and HTI are nearly the same as shown in Fig. 4).

4.1. Ignition in 1D planar configuration

Autoignition processes with different values of non-dimensional temperature gradient, ξ, are simulated. The typical autoignition process at $\xi = 4$ is discussed below since it involves complex interactions among different ignition stages and pressure waves. The results are shown in Fig. 5. It is observed that autoignition of the hot spot generates a first detonation wave (denoted as D1 in Fig. 5) and a strong pressure/shock wave (marked by open circles P on lines #5 and #6 in Fig. 5a) in front of it. As will be shown later, the detonation wave and the preceding pressure/shock wave are caused by local high-temperature ignition (HTI) and intermediate-temperature ignition (ITI), respectively. Due to the reinforcement by local heat release from chemical reactions, the ITI-induced pressure wave eventually
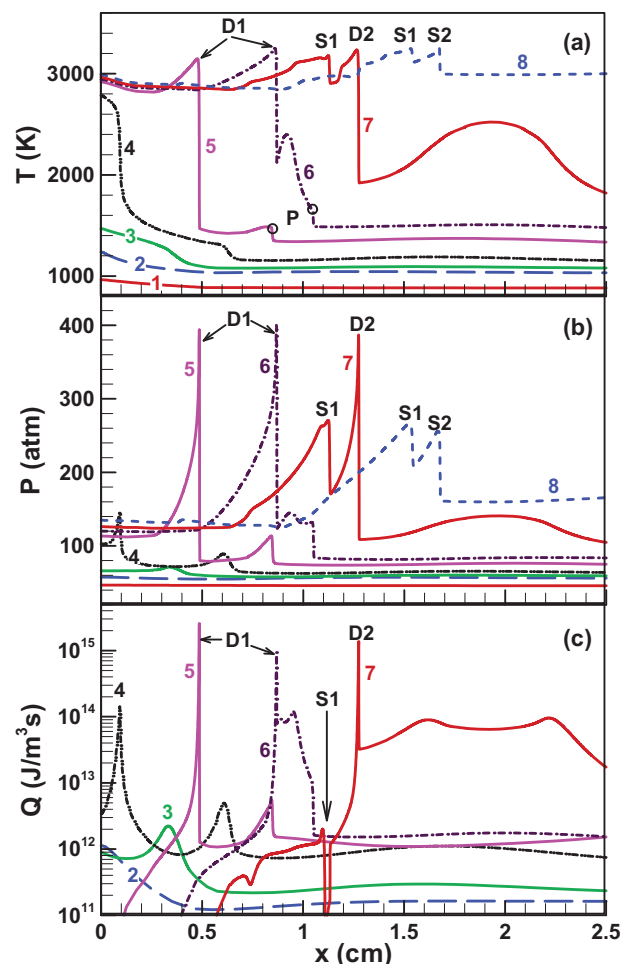

Fig. 5. Temporal evolution of (a) temperature, (b) pressure, and (c) heat release rate distributions in 1D planar configuration with $\xi = 4$ ($dT_0/dx = -0.48$ K/mm), $T_m = 780$ K, and $x_s = 0.5$ cm. The time sequence is 1: 1000 μs, 2: 1025 μs, 3: 1030 μs, 4: 1034 μs, 5: 1037 μs, 6: 1039 μs, 7: 1041 μs, 8: 1044 μs.

evolves into a shock wave. This pressure wave and the subsequent shock wave are therefore called as ITI pressure wave and ITI shock wave, respectively.

The propagation of pressure/shock waves is marked in Fig. 6, which plots the enlarged pressure distributions shown in Fig. 5. Besides ITI pressure/shock wave, it is observed that there is another weak pressure wave ahead of the ITI pressure/shock wave, which is marked by open squares in Fig. 6. This weak pressure wave is caused by local low-temperature ignition (LTI) and therefore it is referred to as LTI pressure wave. Since the heat release of LTI is much lower than that of ITI and the excitation time of LTI is apparently longer than that of ITI (see the inset in Fig. 2), the LTI pressure wave is much weaker than ITI pressure wave. The temperature increases and thereby the ignition delay reduces when the mixture is compressed by these pressure waves. Consequently, the mixture between the ITI pressure wave and detonation wave D1 reacts rapidly (from line #5 to line #6 in Fig. 5), and thereafter produces a second detonation wave D2 (line #7 in Fig. 5). Meanwhile, the first detonation wave D1 degenerates into a shock wave (S1) since the reactants in the upstream of D1 are consumed by autoignition and D2 (line #7 in Fig. 5). Finally, autoignition occurs in the mixture in front of the second detonation wave D2 and it generates two supersonic autoignition fronts propagating in the opposite directions (line #7 in Fig. 5). After the collision between the second detonation wave D2 and the supersonic autoignition front propagating to the left, all the reactants are consumed and thereby D2 becomes a shock wave S2 (line #8 in Fig. 5).
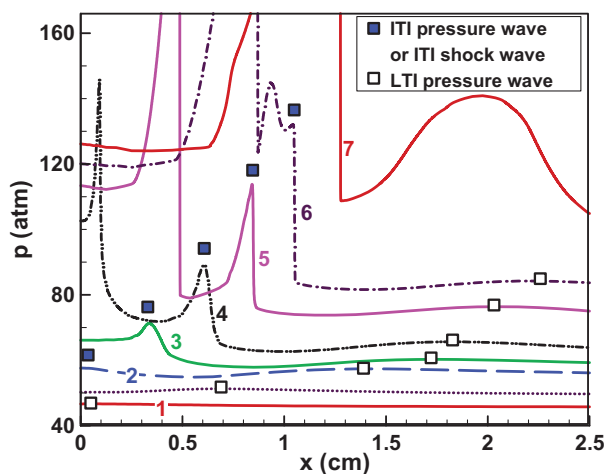
Fig. 6. Enlarged display of pressure distributions shown in Fig. 5(b). The local peak pressures are marked by open (for LTI) and closed (for ITI) squares. The time sequence is the same as that in Fig. 5.

In order to demonstrate that the LTI pressure wave and ITI pressure/shock wave shown in Fig. 6 are respectively induced by the LTI and ITI inside the hot spot, we consider the case in which the mixture initially surrounding the hot spot is inert. The inert surrounding mixture has zero reaction rate; but it has the same thermal and transport properties as normal reactive nC_7H_{16}/air mixture. The interface between the reactive mixture inside the hot spot and the inert surrounding mixture is initially located at $x = x_s = 0.5$ cm and it is continuously pushed toward the right side. The initial temperature distribution is not changed (i.e., $\xi = 4$, $T_m = 780$ K, and $x_s = 0.5$ cm). The results are plotted in Figs. 7 and 8. Figure 7 shows that the first detonation D1 is developed and it propagates to the right, which is similar to D1 shown in Fig. 5 for normal reactive mixture. In front of D1, there is a pressure wave propagating at the local sound speed. This pressure wave is caused by the ITI inside the hot spot since there is no heat release from the inert sounding mixture. Unlike the case considering normal reactive nC_7H_{16}/air mixture shown in Fig. 5, Fig. 7 shows that the detonation wave D1 catches up with the ITI pressure wave. This is because the ITI pressure wave propagates into the inert surrounding mixture and there is no reaction–pressure wave interaction to make it become a second detonation D2 as that in Fig. 5 for normal reactive surrounding mixture. The LTI pressure wave is depicted by the enlarged display shown in Fig. 8. Both LTI pressure wave and ITI pressure wave are shown to appear even when the chemical reaction is disabled for the mixture initially outside the hot spot. This indicates that LTI pressure wave and ITI pressure wave are indeed induced respectively by LTI and ITI inside the hot spot.

It is noted that only in Figs. 7 and 8 is inert surrounding mixture considered. All other figures show the results for normal reactive surrounding mixture (i.e., the mixture in the whole domain is reactive).

The change of reaction front, x_f, with time, t, is plotted in Fig. 9 for the case shown in Fig. 5. The reaction front, x_f, is defined as the location where temperature reaches 2000 K. Nearly the same results are obtained when the reaction front is defined as the position of local peak heat release rate. It is observed that at certain time period, multiple reaction fronts exist and propagate in opposite directions due to local autoignition caused by ITI or LTI pressure waves. The inset in Fig. 9 depicts the reaction front propagation trajectories, cd and cb, which are caused by the ITI pressure/shock wave (see line #6 in Figs. 5 and 6). The left-propagating reaction front, cb, collides with the first detonation wave D1; and the right-propagating reaction front, cd, evolves into the second detonation wave D2. The propagating speed of D1 and D2 is around 1720 m/s, which is different from the C–J detonation speed of 1855 m/s for stoichiometric nC_7H_{16}/air at $T_0 = 780$ K
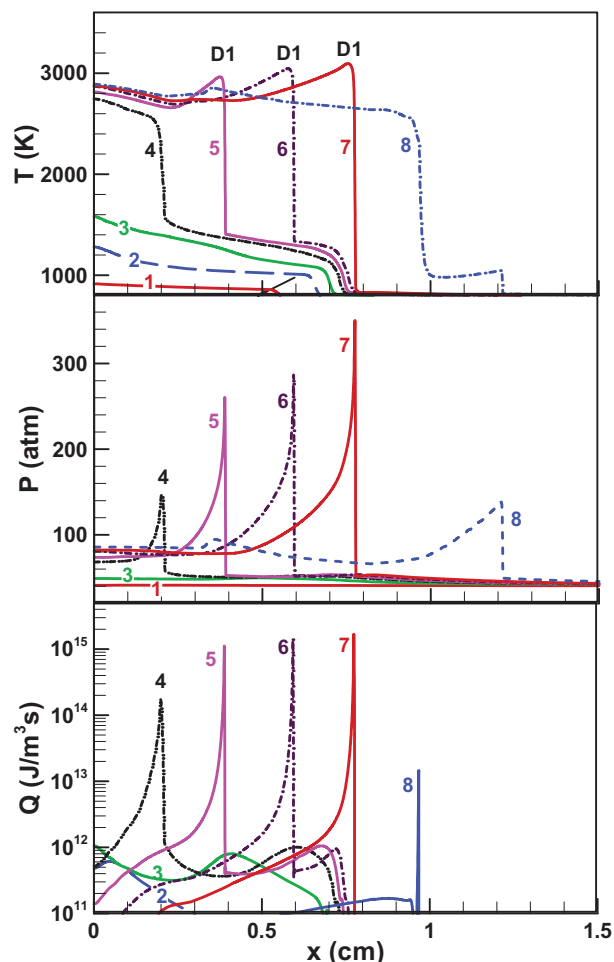

Fig. 7. Results for autoignition in 1D planar configuration with $\xi = 4$ ($dT_0/dx = -0.48$ K/mm), $T_m = 780$ K, and $x_s = 0.5$ cm (same as those in Fig. 5). The mixture initially outside the hot spot (i.e., $x > x_s$) is inert (i.e., the chemical reaction is artificially disabled throughout the simulation). The time sequence is 1: 1017 μs, 2: 1075 μs, 3: 1086 μs, 4: 1089 μs, 5: 1090 μs, 6: 1091 μs, 7: 1092 μs, 8: 1096 μs. At $t = 1096$ μs (lines #8), the interface between the reactive mixture and the inert mixture is pushed from $x = x_s = 0.5$ cm to $x = 0.96$ cm due to expansion.

and $P_0 = 40$ atm. Such small difference (around 7%) is reasonable since D1 and D2 occur after LTI and ITI. It is also noticed that the detonation speed of D1 and D2 is much lower than that of the autoignitive reaction fronts, cb and cd.

The autoignition caused by LTI pressure wave occurs in front of the second detonation wave D2 and it generates two supersonic reaction fronts, fg and fe, propagating in the opposite directions (see Fig. 9 and line #7 in Fig. 5). The left-propagating reaction front, fe, meets the second detonation wave D2; and the right-propagating reaction front, fg, does not evolve into a detonation wave since the rest of unburned mixture is quickly consumed. The propagation speed of these two supersonic reaction fronts, fg and fe, is above 10,000 m/s, which is much larger than sound speed and detonation speed. Therefore, these supersonic reaction fronts are controlled only by local autoignition (chemical reactions) and the pressure wave cannot be coupled with the local autoignition/reaction.

To further reveal the chemical–gas dynamic interaction during the supersonic reaction front propagation, the thermal states of flow particles at different initial locations are traced [53]. First, the position of a particle is updated by its current flow speed multiplying the time step size of 4×10^{-10} s; then, the thermal states of this particle are obtained from linear extrapolation of corresponding states at its two neighboring grids. For the case shown in Fig. 5, three flow particles
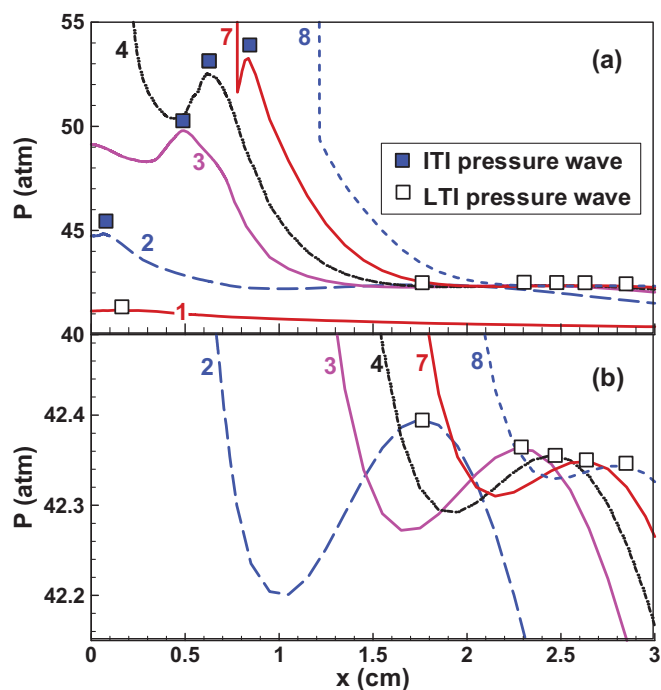
Fig. 8. Enlarged display of pressure distributions shown in Fig. 7(b). The local peak pressures are marked by open (for LTI) and closed (for ITI) squares. The time sequence is the same as that in Fig. 7.
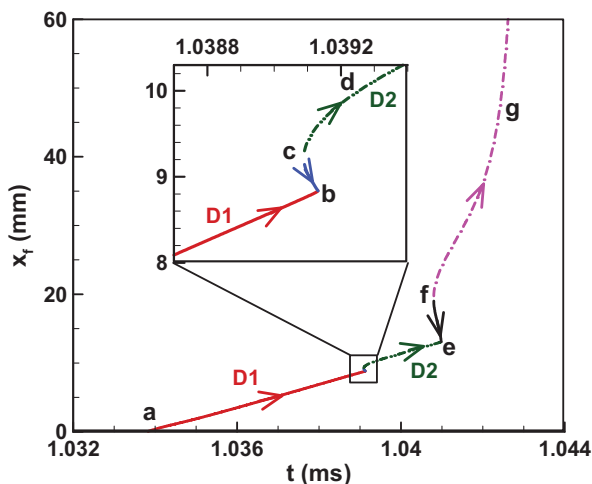

Fig. 9. Change of reaction front, x_f, with time, t. The conditions are the same as those for Fig. 5 (i.e., $\xi = 4$, $dT_0/dx = -0.48$ K/mm, $T_m = 780$ K, and $x_s = 0.5$ cm). The arrow indicates the propagation direction (i.e., increase of time t). The propagation speed of detonation waves D1 and D2 is around 1720 m/s.

initially at $x_0 = 0.3$ cm (inside the hot spot), $x_0 = 0.9$ cm (around the autoignition position caused by the ITI shock wave, see line #6 in Figs. 5 and 6) and $x_0 = 1.1$ cm (the position passed by the second detonation wave D2) are tracked. The diagrams of pressure versus specific volume, P–v, for these three flow particles are depicted in Fig. 10. Besides, the evolution of pressure, P–t, and that of heat release rate, Q–t, are also shown for reference.

Fig. 10(a) shows typical evolution of thermal states of a flow particle inside the hot spot ($x_0 = 0.3$ cm). Points a, b and c denote the moments of peak heat release rate, which respectively correspond to three ignition stages of LTI, ITI and HTI. The lower part of the P–v line (before and slightly after point a) with increasing pressure and decreasing density (the inverse of v) represents a local autoignition and

expansion process dominated by LTI. After LTI, this flow particle is compressed by ITI pressure wave propagating from its left side. The heat release due to local ITI also increases the pressure. Therefore, the pressure and density of this flow particle both increase (see the part between points a and b on the P–v line). After point b, the pressure decreases slightly due to the fact that the expansion effect dominates over the ITI heat release effect. It is noticed that the pressure at point b is much larger than that at point a ($P_a = 50$ atm, $P_b = 71.5$ atm). The mixture immediately behind the right-propagating ITI pressure wave is compressed to react rapidly and, in turn, further reinforce the pressure wave. Therefore, there is mutual enforcement between the local heat release due to intermediate-temperature chemistry and the ITI pressure wave. The upper part of the P–v line is similar to that for a classical ZND detonation structure. The upper part of the curve between points b and c on the P–v diagram is the Hugoniot line. However, it corresponds to mixture after LTI and ITI instead of unburned fresh mixture. HTI occurs inside the first detonation wave D1 which has already developed (from line #4 to line #5 in Fig. 5), indicating that the first detonation wave D1 is driven by HTI instead of LTI or ITI. Therefore, the evolution process of this flow particle inside the hot spot is sequentially dominated by LTI, ITI pressure wave and ITI, and detonation wave D1 with HTI.

To show the autoignition process occurring at the position between the ITI shock wave and the first detonation wave, D1 (see line #6 in Fig. 5), Fig. 10(b) plots the evolution of thermal states of the flow particle initially at $x_0 = 0.9$ cm. Again, points a, b and c respectively correspond to three ignition stages of LTI, ITI and HTI. The part of P–v line around point a represents the compression–expansion process, which is caused by the passage of LTI pressure and local LTI heat release. After that, the right-propagating ITI pressure wave has already evolved into a shock wave when it passes the flow particle initially at $x_0 = 0.9$ cm. This is marked on the P–v diagram shown in Fig. 10(b). It is noticed in Fig. 10(b) that the local ITI heat release occurs before the arrival of the ITI shock wave. Therefore, the ITI shock wave and local ITI are not coupled with each other and the second detonation wave, D2, is not yet developed at this flow particle. HTI (point c in Fig. 10b) occurs after the passage of the ITI shock wave. Since the reactants is completely consumed by HTI before the arrival of the first detonation wave D1, D1 degenerates to a shock wave S1 and S1 passes the products of local HTI. Therefore, the evolution process of the flow particle initially at $x_0 = 0.9$ cm is sequentially dominated by LTI pressure wave and LTI, ITI, ITI shock wave, HTI, and shock wave S1.

Lines #6 and #7 in Fig. 5 indicate that the local autoignition caused by ITI pressure wave generates another detonation wave D2. In order to get more details on the development of detonation wave D2, Fig. 10(c) shows the evolution of thermal states of the flow particle initially at $x_0 = 1.1$ cm. The LTI and ITI stages are similar to those shown in Fig. 10(b) for the flow particle initially at $x_0 = 0.9$ cm. However, Fig. 10(c) shows that after ITI around point b, there appears the detonation wave D2 instead of the ITI shock wave shown in Fig. 10(b). The maximum HTI heat release rate (point c in Fig. 10c) is reached after the shock wave (which corresponds to curve between points b and c on the P–v diagram). This indicates that similar to detonation wave D1, D2 is also maintained by high-temperature reactions. After D2, the flow particle is compressed by the shock wave S1. Therefore, the evolution process of the flow particle initially at $x_0 = 1.1$ cm is sequentially dominated by LTI pressure wave and LTI, ITI, detonation wave D2 maintained by HTI, and shock wave S1.

The P–v diagrams for the above three flow particles as well as the fourth one initially at $x_0 = 8$ cm are shown in Fig. 11 for comparison. Lines #7 and #8 in Fig. 5 indicate that the flow particle initially at $x_0 = 8$ cm is passed by the autoignition front (i.e., nearly constant volume ignition occurs) and thereby it corresponds to a vertical line in the P–v diagram in Fig. 11. Moreover, it is observed that the P–v line for detonation wave D1 passing the particle initially at $x_0 = 0.3$ cm is similar to that for detonation wave D2 passing the particle initially
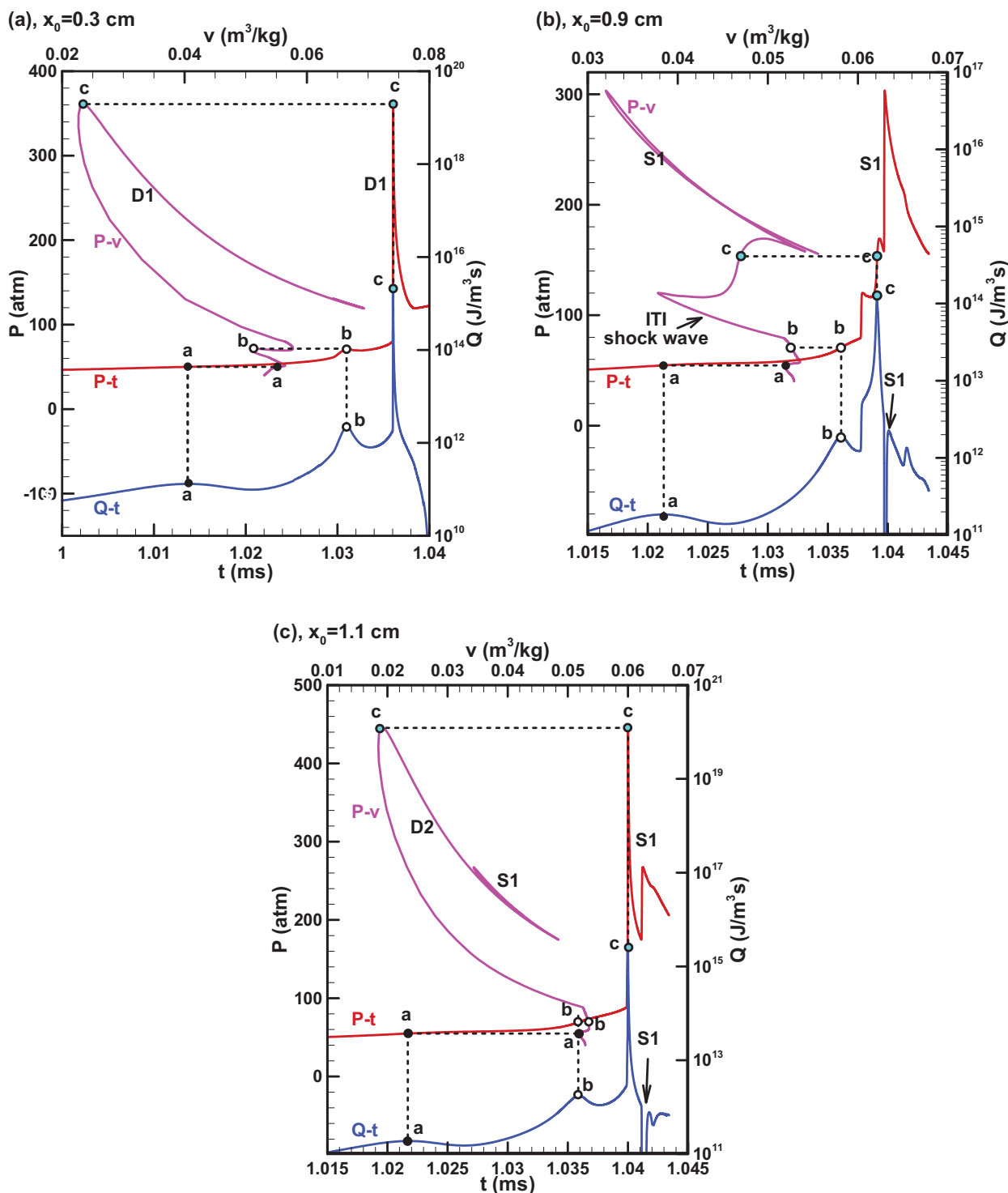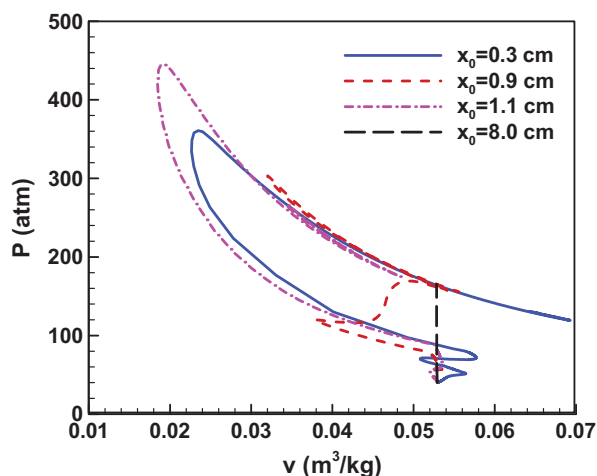
Fig. 10. *P–v* (pressure versus specific volume), *P–t* (pressure versus time), and *Q–t* (heat release rate versus time) diagrams for particles initially at (a) $x_0 = 0.3$ cm, (b) $x_0 = 0.9$ cm, and (c) $x_0 = 1.1$ cm. The conditions are the same as those for Fig. 5 (i.e., $\xi = 4$, $dT_0/dx = -0.48$ K/mm, $T_m = 780$ K, and $x_s = 0.5$ cm).

at $x_0 = 1.1$ cm. As mentioned before, this is because both detonation waves D1 and D2 are maintained by heat release from HTI.
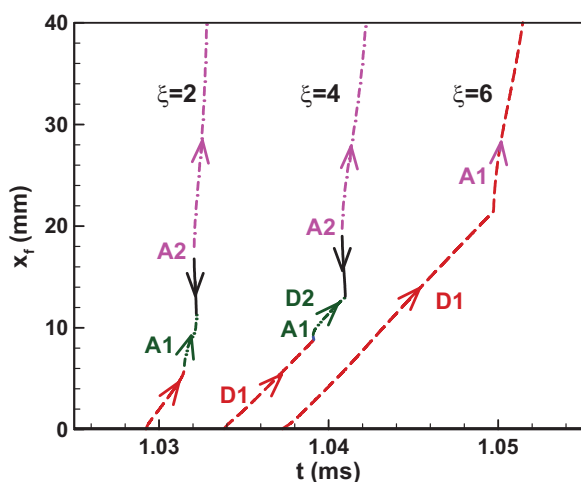
The above discussion focuses on the typical case with $\xi = 4$, in which complex interactions among LTI, ITI, HTI and corresponding pressure waves are observed. Simulation results indicate that with the change of temperature gradient inside the hot spot, such interactions may be strengthened or weakened and thereby the mode of supersonic reaction front propagation changes. The reaction front history for different temperature gradients is compared in Fig. 12.

When the non-dimensional temperature gradient is reduced from $\xi = 4$ to $\xi = 2$, the autoignition front propagates faster according to Eq. (19). This weakens the coherent interaction between HTI and pressure wave; and thereby no detonation can be developed for $\xi = 2$. (It is noted that the critical condition for detonation development is not $\xi = 1$. As shown in [20,24], detonation occurs when ξ reaches some value above unity.) Similar observation was made in previous simulations (e.g., [20,24]). However, due to the presence of low- and intermediate-temperature reactions, the LTI and ITI
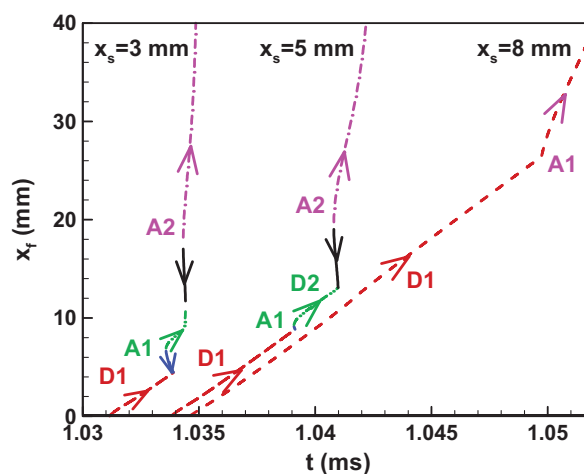
Fig. 11. P–v diagram for particles at different initial positions. The conditions are the same as those for Fig. 5 (i.e., $\xi = 4$, $dT_0/dx = -0.48$ K/mm, $T_m = 780$ K, and $x_s = 0.5$ cm).

Fig. 13. Change of reaction front, x_f, with time, t, for 1D planar configuration with $\xi = 4$ and different hot spot sizes of 3, 5 and 8 mm. The arrow indicates the corresponding propagation direction. The propagation speed of detonation wave D1 is around 1700 m/s.

Fig. 12. Change of reaction front, x_f, with time, t, for 1D planar configuration with different temperature gradients inside the hot spot. The arrow indicates the corresponding propagation direction. The propagation speed of detonation waves D1 and D2 for $\xi = 4$ is around 1720 m/s, and that of detonation wave D1 for $\xi = 6$ is 1800 m/s.
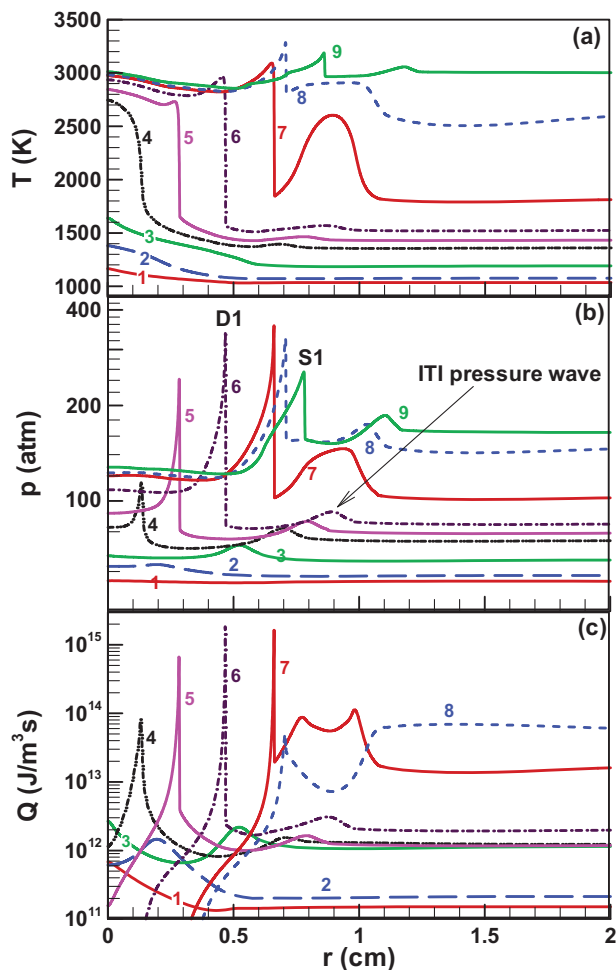
the hot spot size is increased from $x_s = 5$ mm to $x_s = 8$ mm, Fig. 13 shows that only one supersonic autoignition front A1 occurs just in front of detonation wave D1. This is similar to the case of $\xi = 6$ shown in Fig. 12. Therefore, Fig. 13 indicates that the hot spot size affects the reaction–pressure wave interactions and the occurrence of different autoignition and detonation fronts. The characteristic acoustic time is usually defined as the ratio between hot spot size and sound speed [20]. Therefore, the hot spot size affects the value of ε (which is equal to the ratio of acoustic time to excitation time), which is used to determine the autoignition regimes [20,24].

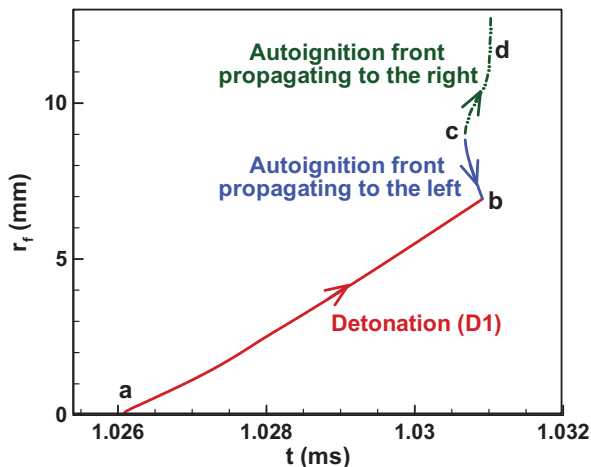### 4.2. Ignition in 1D spherical configuration

In this subsection, we consider ignition from a hot spot in a spherical configuration. In order to compare with the results in Fig. 5 for the planar configuration, we consider the same temperature gradient of $\xi = 4$ in the spherical case. The values for other parameters ($P_0 = 40$ atm, $T_m = 780$ K and $r_s = 0.5$ cm) are also the same. The results are shown in Fig. 14. Unlike the planar case shown in Fig. 5, Fig. 14 shows that for the spherical case, only one detonation wave appears through the entire spherical ignition process. This detonation wave is caused by direct coupling between HTI and its corresponding pressure wave. Therefore, it is similar to detonation wave D1 in the planar case.

The detonation and pressure waves in spherical configuration are much weaker than those in planar configuration. This is due to incessant expansion and attenuation of waves during propagation (i.e., the curvature effect). Therefore, besides the relatively weaker detonation wave D1, Fig. 14 shows that the ITI pressure wave is also much weaker than that in the planar case in Fig. 5. Consequently, the ITI pressure wave is not strong enough to evolve into a shock wave and thereby the second detonation wave D2 does not appear in spherical configuration. Due to the compression of the ITI pressure wave, autoignition occurs in the mixture in front of the detonation wave D1 (see line #7 in Fig. 14) and it generates two supersonic autoignitive wave propagating in the opposite directions. Detonation wave D1 collides with the supersonic autoignitive wave propagating to the left and it becomes a shock wave S1 since all the reactants are consumed (from line #7 to line #8 in Fig. 14).

The reaction front history for the spherical case is shown in Fig. 15. It is observed that the speed of detonation wave D1 in spherical configuration (1550 m/s) is much lower than that in planar configuration (1720 m/s) since the detonation is weakened by the

pressure waves can propagate in front of the conventional reaction front dominated by HTI. Therefore, for the case of $\xi = 2$, Fig. 12 shows that autoignition in front of HTI reaction front occurs twice (marked as A1 and A2 in Fig. 12) and generates new supersonic autoignition fronts propagating in different directions. On the other hand, when the temperature gradient is increased from $\xi = 4$ to $\xi = 6$, the autoignition front propagates slower according to Eq. (19). This enhances the coherent coupling between HTI and pressure wave, which induce a stronger detonation wave D1 propagating faster than that in the case of $\xi = 4$. Fig. 12 shows that unlike the cases of $\xi = 2$ and $\xi = 4$, there is only one supersonic autoignition front for $\xi = 6$ (marked as A1 in Fig. 12) which occurs just in front of detonation wave D1.

For all the results discussed above, the hot spot size is fixed to be 5 mm. In Fig. 13 the results for different hot spot sizes, $x_s = 3, 5$ and 8 mm, are presented. Other parameters ($\xi = 4$, $dT_0/dx = -0.48$ K/mm, $T_m = 780$ K, $P_0 = 40$ atm) are the same as those for the case shown in Fig. 5. Though detonation and autoignition fronts are observed for these three cases, there are differences caused by the change in hot spot size. When the hot spot size is reduced from $x_s = 5$ mm to $x_s = 3$ mm, the second detonation D2 does not occur since the fresh mixture is quickly consumed by autoignition fronts A1 and A2. When

Fig. 14. Temporal evolution of (a) temperature, (b) pressure, and (c) heat release rate distributions in 1D spherical configuration with $\xi = 4$ ($dT_0/dr = -0.48$ K/mm), $T_m = 780$ K, and $r_s = 0.5$ cm. The time sequence is 1: 1015 μs, 2: 1020 μs, 3: 1024 μs, 4: 1027 μs, 5: 1028 μs, 6: 1029 μs, 7: 1030 μs, 8: 1031 μs, 9: 1032 μs.

Fig. 15. Change of reaction front, R_f, with time, t. The conditions are the same as those for Fig. 14 (i.e., $\xi = 4$, $dT_0/dr = -0.48$ K/mm, $T_m = 780$ K, and $r_s = 0.5$ cm). The arrow indicates the propagation direction (i.e., increase of time t). The propagation speed of detonation waves D1 is around 1550 m/s.
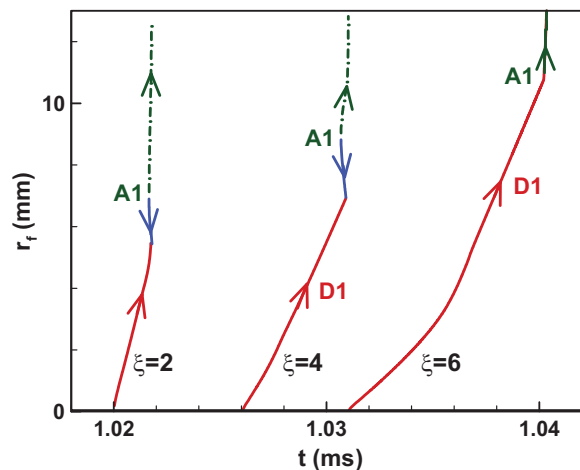
Fig. 16. Change of reaction front, R_f, with time, t, for 1D spherical configuration with different temperature gradients inside the hot spot. The arrow indicates the corresponding propagation direction. The propagation speeds of detonation wave D1 for $\xi = 4$ and $\xi = 6$ are respectively around 1550 m/s and 1630 m/s.

curvature effect. Similar to the planar case, the autoignition caused by ITI pressure wave generates two reaction fronts propagating in the opposite directions (along curves *cd* and *cb* in Fig. 15). The LTI pressure wave causes the autoignition in front of detonation wave D2 in planar configuration, however, does not induce local autoignition in spherical configuration. This is because in spherical configuration, the LTI pressure wave becomes weaker as it propagates outwardly.

We also consider different temperature gradients in spherical configuration and the results are shown in Fig. 16. The influence of temperature gradient is shown to be similar to that for the planar configuration in Fig. 12. At lower non-dimensional temperature gradient of $\xi = 2$, the reaction front propagates faster and no detonation is observed. At higher non-dimensional temperature gradient of $\xi = 6$, first the hot spot generates an autoignitive wave propagating at relatively low speed around 600 m/s; then autoignitive wave accelerates and becomes a detonation wave D1. For these three temperature gradients, local autoignition (marked as A1 in Fig. 16) caused by the ITI pressure wave generates reaction fronts propagating in different directions. Unlike the planar case in Fig. 12, there is no local autoignition caused by the LTI pressure wave. As mentioned before, this is because the LTI pressure wave becomes weaker as it propagates outwardly in spherical configuration. Therefore, the curvature effects changes the modes of supersonic reaction front propagation initiated by a hot spot in *n*-heptane/air mixture with multistage ignition.

It is noted that for all the results discussed above, the initial temperature is $T_m = 780$ K (at which the critical temperature gradients for LTI, ITI and HTI are nearly the same, see Fig. 4). Simulations are also conducted for the initial temperature of $T_m = 840$ K (at which the critical temperature gradient for LTI is different from those for ITI and HTI, see Fig. 4) and $T_m = 900$ K (which is in the NTC regime, see Fig. 4). Zero-dimensional simulation results for homogeneous ignition process indicates that the intermediate-temperature ignition stage is suppressed as the initial temperature increases. As a result, in 1D ignition from a hot spot with $T_m = 840$ K, the ITI pressure wave is found to be too weak to evolve into a shock wave and thereby a second detonation wave is not observed. For $T_m = 900$ K within the NTC regime, a cool spot with positive temperature gradient should be used to induce supersonic reaction front propagation [24]. Moreover, the ITI is fully suppressed and only LTI and HTI occurs for $T_m = 900$ K. Therefore, only one detonation wave is induced (more details are shown in our previous study [24]).

5. Conclusions

One-dimensional simulations are conducted to study the autoignition and supersonic reaction front propagation initiated by a hot spot. The stoichiometric n-heptane/air mixture with low initial temperature and multistage ignition is considered. Results for 0D homogeneous ignition indicate that there are three ignition stages, LTI, ITI and HTI, which are dominated by low-, intermediate- and high-temperature chemistries, respectively. At low initial temperature, the critical temperature gradients corresponding to three ignition stages are found to be nearly the same, indicating that it is possible for all these ignition stages to generate strong chemical–acoustic interactions at proper temperature gradient.

The reaction–pressure wave interactions from multistage ignition are first investigated in planar configuration. In a typical case with non-dimensional temperature of $\xi = 4$, multiple pressure waves, shock waves, and detonation waves are observed and they are found to be generated by heat release from different ignition stages and reaction–pressure wave interactions. The autoignition of the hot spot first generates a detonation wave (D1) and two preceding pressure waves (LTI and ITI pressure waves). Then the ITI pressure wave evolves into a shock wave and the mixture between the shock wave and detonation wave D1 reacts rapidly, which generates a second detonation wave D2 due to the coherent coupling between local heat release and pressure wave. Finally, local autoignition induced by the compression of LTI pressure wave occurs in front of detonation wave D2; and it generates supersonic autoignition waves that cause rapid ignition of the rest of the mixture. Besides, the temperature gradient of the hot spot is found to affect the interaction among multistage ignition and pressure waves. Therefore, change in temperature gradient causes change in the mode of supersonic autoignition front propagation. With the increase of temperature gradient, the coherent coupling between HTI and pressure wave is enhanced, which results in a stronger detonation wave D1 and disappearance of the second detonation wave D2.

Comparison between the results in spherical and planar configurations indicates that supersonic reaction front propagation is strongly affected by geometry. Similar to the planar case, detonation wave D1 and LTI and ITI pressure waves are also observed in spherical configuration. However, the detonation and pressure waves in spherical configuration are much weaker than those in planar configuration due to the curvature effects. Consequently, in spherical configuration, the ITI pressure wave is not strong enough to evolve into a shock wave and thus the second detonation wave D2 does not appear.

References

[1] J.B. Heywood, Internal Combustion Engines Fundamentals, McGraw Hill, New York, 1988.
[2] J. Zaccardi, L. Duval, A. Pagot, J. Engines 2 (2009) 1587–1600.
[3] G.T. Kalghatgi, D. Bradley, Int. J. Engine Res 13 (2012) 399–414.
[4] Z. Wang, H. Liu, T. Song, Y.L. Qi, X. He, S.J. Shuai, J.X. Wang, Int. J. Engine Res 16 (2015) 166–180.
[5] J.Y. Pan, G.Q. Shu, H.Q. Wei, Combust. Sci. Technol. 186 (2014) 192–209.
[6] G.T. Kalghatgi, Proc. Combust. Inst. 35 (2015) 101–115.
[7] G.T. Kalghatgi, Fuel/engine interactions, SAE Int. (2013).
[8] D. Bradley, Philos. Trans. R. Soc. A 370 (2012) 689–714.
[9] Z. Wang, Y. Qi, X. He, J. Wang, S. Shuai, C.K. Law, Fuel 144 (2015) 222–227.
[10] Z. Wang, Y. Wang, R.D. Reitz, Energ. Fuel. 26 (2012) 7107–7119.
[11] Y.B. Zel'dovich, V.B. Librovich, G.M. Makhviladze, G.I. Sivashinsky, Acta Astronaut. 15 (1970) 313–321.
[12] Y.B. Zel'dovich, Combust. Flame 39 (1980) 211–214.
[13] J.F. Clarke, Prog. Energ. Combust. 15 (1989) 241–271.
[14] A.M. Khokhlov, E.S. Oran, J.C. Wheeler, Combust. Flame 108 (1997) 503–517.
[15] A.K. Kapila, D.W. Schwendeman, J.J. Quirk, T. Hawa, Combust. Theory Model 6 (2002) 553–594.
[16] G.J. Sharpe, M. Short, J. Fluid Mech. 476 (2003) 267–292.
[17] M.D. Kurtz, J.D. Regele, Combust. Theory Model 18 (2014) 532–551.
[18] H.J. Weber, A. Mack, P. Roth, Combust. Flame 97 (1994) 281–295.
[19] D. Bradley, C. Morley, X.J. Gu, D.R. Emerson, SAE (2002) 2002-01-2868.
[20] X.J. Gu, D.R. Emerson, D. Bradley, Combust. Flame 133 (2003) 63–74.
[21] M.A. Liberman, A.D. Kiverin, M.F. Ivanov, Phys. Lett. A 375 (2011) 1803–1808.
[22] M.A. Liberman, A.D. Kiverin, M.F. Ivanov, Phys. Rev. E 85 (2012) 056312.
[23] A.D. Kiverin, D.R. Kassoy, M.F. Ivanov, M.A. Liberman, Phys. Rev. E 87 (2013) 033015.
[24] P. Dai, Z. Chen, S.Y. Chen, Y.G. Ju, Proc. Combust. Inst. 35 (2015) 3045–3052.
[25] Y.G. Ju, W.T. Sun, M.P. Burke, X.L. Gou, Z. Chen, Proc. Combust. Inst. 33 (2011) 1245–1251.
[26] J.B. Martz, H. Kwak, H.G. Im, G.A. Lavoie, D.N. Assanis, Proc. Combust. Inst. 33 (2011) 3001–3006.
[27] W. Sun, S.H. Won, X. Gou, Y. Ju, Proc. Combust. Inst. 35 (2015) 1049–1056.
[28] R. Sankaran, H.G. Im, E.R. Hawkes, J.H. Chen, Proc. Combust. Inst. 30 (2005) 875–882.
[29] J.H. Chen, E.R. Hawkes, R. Sankaran, S.D. Mason, H.G. Im, Combust. Flame 145 (2006) 128–144.
[30] G. Bansal, H.G. Im, Combust. Flame 158 (2011) 2105–2112.
[31] C.S. Yoo, T.F. Lu, J.H. Chen, C.K. Law, Combust. Flame 158 (2011) 1727–1741.
[32] M.B. Luong, Z.Y. Luo, T.F. Lu, S.H. Chung, C.S. Yoo, Combust. Flame 160 (2013) 2038–2047.
[33] S.O. Kim, M.B. Luong, J.H. Chen, C.S. Yoo, Combust. Flame 162 (2015) 717–726.
[34] Z. Chen, M.P. Burke, Y.G. Ju, Proc. Combust. Inst. 32 (2009) 1253–1260.
[35] Z. Chen, Combust. Flame 157 (2010) 2267–2276.
[36] R.J. Kee, F.M. Rupley, J.A. Miller, A Fortran Program For Modeling Steady Laminar One-Dimensional Premixed Flames, Sandia National Laboratory Report SAND89-8009B, 1989.
[37] S.L. Liu, J.C. Hewson, J.H. Chen, H. Pitsch, Combust. Flame 137 (2004) 320–339.
[38] R.J. Kee, J.F. Grcar, M.D. Smooke, J.A. Miller, CHEMKIN-II: A Fortran Package for the Analysis of Gas-Phase Chemical Kinetics, Sandia National Laboratory Report SAND85-8240, 1985.
[39] G. Strang, SIAM J. Numeric. Anal. 5 (1968) 506–517.
[40] P.N. Brown, G.D. Byrne, A.C. Hindmarsh, SIAM, J. Sci. Stat. Comput. 10 (1989) 1038–1051.
[41] X.L. Gou, W.T. Sun, Z. Chen, Y.G. Ju, Combust. Flame 157 (2010) 1111–1121.
[42] X.L. Gou, Z. Chen, W.T. Sun, Y.G. Ju, Combust. Flame 160 (2013) 225–231.
[43] Z. Chen, M.P. Burke, Y.G. Ju, Proc. Combust. Inst 33 (2011) 1219–1226.
[44] Z. Chen, Combust. Flame 158 (2011) 291–300.
[45] W.K. Zhang, Z. Chen, W.J. Kong, Combust. Flame 159 (2012) 151–160.
[46] W.K. Liang, Z. Chen, F. Yang, H.Q. Zhang, Proc. Combust. Inst. 34 (2013) 695–702.
[47] H. Yu, W. Han, J. Santner, X. Gou, C.H. Sohn, Y. Ju, Z. Chen, Combust. Flame 161 (2014) 2815–2824.
[48] Z. Chen, Combust. Flame 162 (2015) 2242–2253.
[49] Z. Zhao, M. Chaos, A. Kazakov, F.L. Dryer, Int. J. Chem. Kinet 40 (2008) 1–18.
[50] C.K. Law, P. Zhao, Combust. Flame 159 (2012) 1044–1054.
[51] H.A. El-Asrag, Y.G. Ju, Combust. Flame 161 (2014) 256–269.
[52] P. Zhao, C.K. Law, Combust. Flame 160 (2013) 2352–2358.
[53] R. Zhou, J.P. Wang, Combust. Flame 159 (2012) 3632–3645.
[54] H.G. Im, P. Pal, M.S. Wooldridge, A.B. Mansfield, Combust. Sci. Technol. 187 (2015) 1263–1275.
[55] K.P. Grogan, S.S. Goldsborough, M. Ihme, Combust. Flame 162 (2015) 3071–3080.